Statistical studies of plasma structuring in the auroral ionosphere by the Swarm satellites

L.M. Buschmann[1], L.B.N. Clausen[1], A. Spicher[2], M.F. Ivarsen[1,3], W.J. Miloch[1]

[1]University of Oslo, Department of Physics
[2]UiT - The Arctic University of Norway, Institute for Physics and Technology, Tromsø, Norway
[3]University of Saskatchewan, Saskatoon, Saskatchewan, Canada
[1]Postboks 1048, 0316 Oslo, Norway

Key Points:

- Analysis of the power spectral density suggests a disconnection of double slope occurrence rate and irregularity power within certain scales.
- ROTI data are similar to the integrated power from the density PSD but shows higher elevation within the cusp and nightside auroral oval
- The strongest B_y fluctuations are found within the cusp for all seasons and both hemispheres, and are co-located with strong ROTI values.

Corresponding author: L.M. Buschmann, `lisa.buschmann@fys.uio.no`

Abstract

This study uses several years of 16 Hz density measurements, field-aligned current, 50 Hz magnetic field data and ROTI data from the Swarm mission to perform long term statistics of plasma structuring in the polar ionosphere. The timeframe covers more than two years near the 24th solar cycle peak. The data covers the polar cap, auroral oval and mid-latitudes with an emphasis on high latitudes. We present power spectral densities (PSD) of electron density irregularities and magnetic field for one-minute intervals. These PSD were characterized by the probability of a slope steepening, and by integrating the power deposited within different frequency intervals. For the electron density, we observe seasonal dependencies for both the integrated power and slope characteristics. While the slope probability, especially within the polar cap, varies with solar EUV-radiation, the integrated power is strongest around the equinoxes. Additionally, while we found similar results for the slope probability for both hemispheres, the integrated power exhibits strong hemispheric asymmetries with stronger enhancements within local summer in the southern hemisphere. The ROTI data shows a similar seasonal variability as the integrated power from the density PSD, in both seasonal dependency and interhemispheric variability. However, for the ROTI data the strongest fluctuations were found within the nightside auroral oval and the cusp region. For the PSD of the magnetic field data, we obtain the strongest enhancements within the cusp for all seasons and all hemispheres. These enhancements are co-located with the highest ROTI values.

1 Introduction

Auroral particle precipitation is believed to be a major source of large scale irregularities in the plasma of the cusp and night-side auroral oval (Kelley et al., 1982; Moen et al., 2013, 2002). Precipitating electrons can protrude into the ionosphere in these regions and function as a source of free energy. Large-scale irregularities that evolve in the cusp can follow the polar convection pattern towards the night side through the polar cap (PC) and constitute a crucial factor for the development of structures in the polar cap. The most noteworthy of these structures are polar cap patches (PCP).

PCP can be defined as areas with scales between 100-1000 km which have at least twice the density of the background plasma. These patches are generated when high density solar-EUV produced plasma on the dayside ionosphere enters the polar cap ((Carlson, 2012; Crowley et al., 1996) and references therein). When these structures travel through the PC, they can be broken down to smaller scales, in a so-called turbulent cascade. Several sources have been proposed to explain the formation of these irregularities, including the gradient drift instability (GDI) and the Kelvin-Helmholtz instability (KHI) (Kintner & Seyler, 1985; Tsunoda, 1988; Basu et al., 1990; Keskinen & Ossakow, 1983; Carlson, 2012). The GDI affects primarily the trailing edge of PCP as the background plasma flow is parallel to the gradient of the electron density (Tsunoda, 1988). On the other hand, the KHI is driven by velocity shears in the plasma. Lately, a two-step process has been proposed in which patches are first structures by shear driven instabilities (e.g the KHI) in the first minutes after the patch enters the PC. In a second step the GDI is then taking over and further structuring the patch into decameter scale irregularities (Carlson et al., 2007; Carlson, 2012; Moen et al., 2012, 2013; Hosokawa et al., 2013).

Several studies have been conducted with focus on PCP, showing a seasonal dependency of the occurrence of irregularities. Generally, a higher occurrence of patches has been found in the northern hemisphere (NH) during winter season (Chartier et al., 2018; Jin & Xiong, 2020). Overall, polar cap patches are more subdued in summer due to the background plasma from elevated EUV ionization (Spicher et al., 2017). As the majority of these studies have been conducted in the NH, less studies involve the southern hemisphere with contradictory results (Spicher et al., 2017; Chartier et al., 2018, 2019; Jin & Xiong, 2020; David et al., 2019; Kagawa et al., 2021).

When these larger scale structures are broken down to smaller scales, they can cause problems for global navigation satellite systems (GNSS). Scintillations, which are rapid

temporal fluctuations in phase and amplitude in trans-ionospheric GNSS signals, can be detrimental for navigation accuracy or signal acquisition (Kintner et al., 2007; Yeh & Liu, 1982; Basu et al., 1990; Tsunoda, 1988). It has been shown that strong phase scintillations can be related to particle precipitation in the cusp aurora (Jin et al., 2015, 2017; Clausen et al., 2016) and that filamentary field-aligned currents (FAC) are co-located with severe phase scintillation in the cusp (Fæhn Follestad et al., 2020). As GNSS become increasingly important, research on plasma irregularities in the ionosphere has intensified in recent years (Kintner et al., 2007; Oksavik et al., 2012; Moen et al., 2012, 2013; Jin et al., 2014; van der Meeren et al., 2015; Jin et al., 2017).

One method to investigate instabilities and turbulence in plasmas is the use of spectral analysis (Frisch & Kolmogorov, 1995). Ionospheric plasma instabilities have been suggested to follow power laws with different mechanisms resulting in different slopes when fitted in a log-log plot (Kintner & Seyler, 1985; Tsunoda, 1988). Previous observations showed that the initial slope, or spectral index, is approximately $-5/3$ before steepening occurs (Kintner & Seyler, 1985). In situ measurements of the ionosphere revealed that plasma fluctuations exhibit a steeper slope at higher frequencies. This slope steepening was first documented for the low-latitude ionosphere using sounding rockets and satellites (Kelley et al., 1982) and is commonly observed in this region (LaBelle et al., 1986; Hysell et al., 1994; Jahn & LaBelle, 1998). The high-latitude F-region has also shown this steepening (Villain et al., 1986; Basu et al., 1990; Spicher et al., 2014; Ivarsen et al., 2019; Di Mare et al., 2021; Ivarsen et al., 2021; Buschmann et al., 2023). The spectral index in the high-latitude ionosphere has been shown to be approximately $-5/3$ at low frequencies and around -3 to -5 at high frequencies. The frequency at which the spectral break occurs has been studied for decades, but is still not fully understood (Tsunoda, 1988). Recently, Ivarsen et al. (2021) used an automated spectral breakpoint algorithm to characterize power spectra from several years of electron density data showing a spectral index of -1.6 on average at larger scales throughout the F-region ionosphere. Additionally, they linked the occurrence of spectral steepening in the polar ionosphere to the level of solar extreme ultraviolet (EUV) radiation and thus the solar zenith angle (SZA), presenting evidence for the dependency of plasma irregularities in the polar cap on the SZA. Lately it has been found that the occurrence of double slopes in the electron density was most prominent in the cusp and immediately poleward of the cusp, while the strongest electron density fluctuations were found just poleward of the cusp (Buschmann et al., 2023; Spicher et al., 2022). Additionally, an analysis of the integrated spectral power in the power spectral density (PSD) showed an increased energy within lower frequencies in presence of particle precipitation, while power in higher frequencies is elevated poleward of the precipitation, suggesting an energy input from electron precipitation into the cusp in frequencies corresponding to kilometer scales, while the energy is cascading to smaller scales in the polar cap.

This study was conducted by using data from the Swarm satellites. An advantage of the Swarm mission, or polar orbiting satellites in general, is that there is coverage over all latitudes. This gives the opportunity to conduct statistical research for large time periods and different latitudes.

Section 3 of this study gives the results for high solar activity. We have analyzed data between 01.10.2014 and 31.12.2016, and between 01.01.2020 and 31.12.2022, to distinguish between differences in the processes for solar maximum and minimum, respectively. However, due to a larger amount of data gaps within the time frame 2020 to 2022 we decided to mainly focus on the years 2014-2016, a period that directly follows the 24th solar cycle peak. For completeness, the results for low solar activity will be given in Appendix A.

2 Methodology and Instrumentation

This study uses data from the Swarm mission, a satellite constellation consisting of three identical satellites (A, B and C) (Friis-Christensen et al., 2006, 2008). We make

use of data from satellites A and C, which are flying side-by-side (1.4° separation in longitude at the equator) at an altitude of around 460 km. The data employed includes the 16 Hz face-plate electron density, the 50 Hz magnetic field data, the field-aligned current data, and the Rate of Change of TEC index (ROTI) from the Ionospheric Plasma Irregularities (IPIR) dataset (Jin et al., 2022). The dataset used covers a period of more than five years, from 01.10.2014 to 31.12.2016, and from 01.01.2020 to 31.12.2022, to distinguish between differences in the processes for solar maximum and minimum, respectively. For our analysis, we only used time intervals where all data-sets were available, thus ensuring that density, magnetic field, FAC, and IPIR data were present for all intervals. We thus cover the majority of the chosen time frame, however, some larger data gaps can be found throughout the data. For the statistical analysis we additionally only used data poleward of ±50° magnetic latitude. For conversion between geographic coordinates to magnetic latitude (MLat) and magnetic local time (MLT) we used magnetic apex coordinates (Emmert et al., 2010; AD, 1995). Additionally, we divided the data into 4 seasonal intervals, comprising 4 time spans between 91 and 92 days around the equinoxes and solstices. This leads to the following seasonal intervals: spring, utilizing data between 04. February and 05. May, summer between 06. May and 05. August, autumn between 06. and 05. November, and winter between 06. November and 03. February.

For the 16 Hz density and 50 Hz magnetic field data, we conducted a spectral analysis using the Logarithmic frequency axis Power Spectral Density (LPSD) method as described in Tröbs and Heinzel (2006). This procedure utilizes the Welch power spectral method. The Welch power spectra is a method of estimating power spectral density by averaging modified periodograms (Welch, 1967). However, while the Welch method is utilizing the same frequency resolution for every Fourier frequency, the LPSD method is adjusting the frequency resolution instead (Tröbs & Heinzel, 2006). As we are mainly interested in fluctuations of magnetic field and density rather than absolute values, we detrended both quantities with a third-order Savitzky-Golay filter for each 1-minute interval prior to the spectral analysis, in order to get information about the small-scale fluctuations only and eliminate influence of seasonal dependencies in the electron density. This method was chosen for removing a more accurate background, though similar results can be achieved by removing a linear trend. For each 1-minute interval we then performed the spectral analysis mentioned above using a Hanning window. The resulting power spectrum can then be described by either one or two linear slopes in a log-log plot, with

$$PSD(f) \propto f^{-p} \tag{1}$$

where p is the slope of the fit and thus $p > 0$. For a power spectrum that is better described with two fits, the equation changes to

$$PSD(f) \propto \begin{cases} f^{-p1}, & for\ f \leq f_{sb} \\ f^{-p2}, & for\ f \geq f_{sb} \end{cases} \tag{2}$$

where f_{sb} is the break point frequency where the slopes p_1 and p_2 of the PSD change, with $p2 > p1$. We plotted the power spectra for each interval using a logarithmic scale and then used an automated slope detection method, which fits one or two slopes to the spectrum using a piece-wise linear Hermite function. The method is described in more detail in Ivarsen et al. (2019, 2021). The threshold which is used to determine if two fitted slopes are considered a double slope is $p_2 - p_1 \geq 0.8$. This threshold has been used in previous works (Ivarsen et al., 2019; Buschmann et al., 2023) and has been determined by repeated testing. Additionally, we set the range in which a break point could be found to frequencies between 0.19 and 7 Hz, which corresponds spatial scales between 1.1 and 40 km, respectively. This range has been chosen, as repeated use of window functions to obtain the PSD decreases power in low frequencies within the PSD (AD, 1995). Two examples of density PSD plots with either a single or double slope are shown in figure 1.
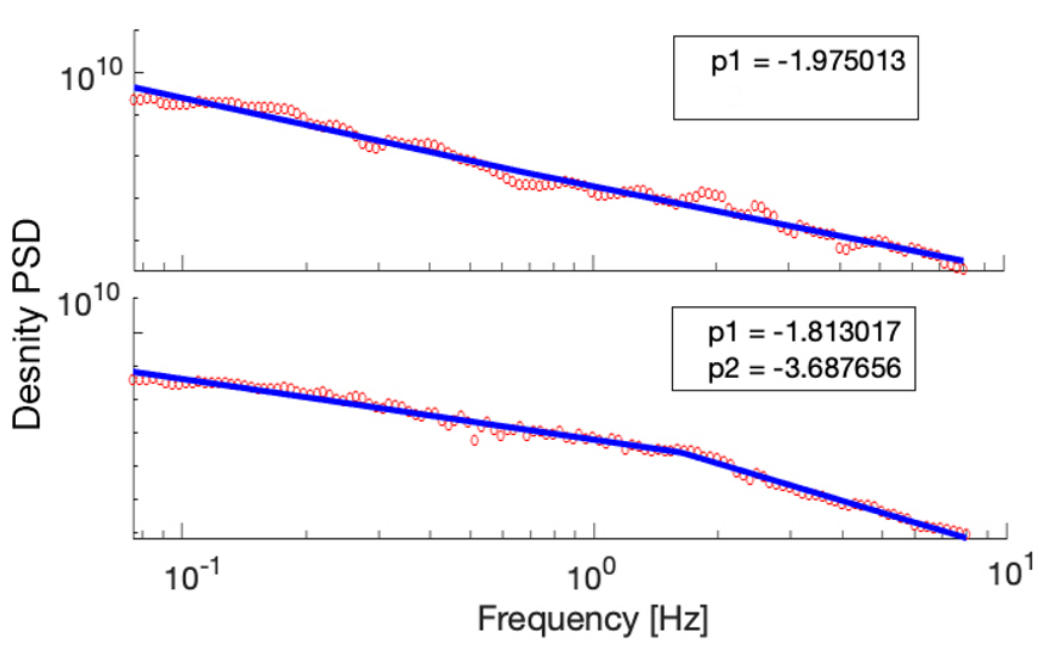
Figure 1. Power-spectral density plot of the electron density. The top plot shows a PSD that is best described with a single fit (single slope, SS), while the bottom plot shows a PSD that is best described by two fits (double slope, DS).

In addition to the slopes and break-point, we analyzed the integrated power within certain frequency intervals in order to compare the power within different spatial scales in different regions. For the density we chose a 1 Hz frequency interval between 1 and 2 Hz, which corresponds to spatial scales between 3.8 and 7.6 km. Additional intervals between 0.1 and 0.6 Hz and 6 and 7 Hz were analysed for comparison. We used a similar method for the analysis of the magnetic field data, only varying in the frequency interval used for detecting break points. As the sampling frequency for the magnetic field is much higher than for the density sampling frequency, we set the interval to frequencies between 0.5 and 23 Hz, corresponding to spatial scales between 0.33 and 15.2 km. The interval chosen for the integrated power analysis was once more a 1 Hz interval, again between 1 and 2 Hz, corresponding to spatial scales between 3.8 and 7.6 km. We decided to use the y-component, or geographic east component in NEC-coordinates, as a proxy for the field-aligned current, as it is not feasible to conduct a spectral analysis on the 1 Hz FAC data in this case, while the magnetic field data is providing 50 Hz resolution. The magnetic field may be converted to the FAC density j_z according to (Fæhn Follestad et al., 2020; Ritter et al., 2013)

$$j_z = \frac{1}{\mu_0 \nu_x} \frac{\Delta B_y}{\Delta t} \tag{3}$$

where ν_x is the velocity perpendicular to the FAC and ΔB_y is the detrended magnetic component parallel to the current sheet (Fæhn Follestad et al., 2020; Wang et al., 2005). We then use the fluctuations is B_y as a means of analyzing the FAC.

Figure 2 shows a sample pass of Swarm A over the northern hemisphere on the 2. November 2014 between 13:09 and 13:41 UT. The trajectory of the satellite can be seen in the upper right corner of figure 2. The figure shows the electron density (panel a), FAC (panel b), magnetic field components (panel c), mROD and mROT (panels d and e) with their corresponding sampling frequencies (16 Hz for panel a, 1 Hz for panels b, d and e, and 50 Hz for panel d). Panels f-h show the slopes, spectral break frequency if applica-
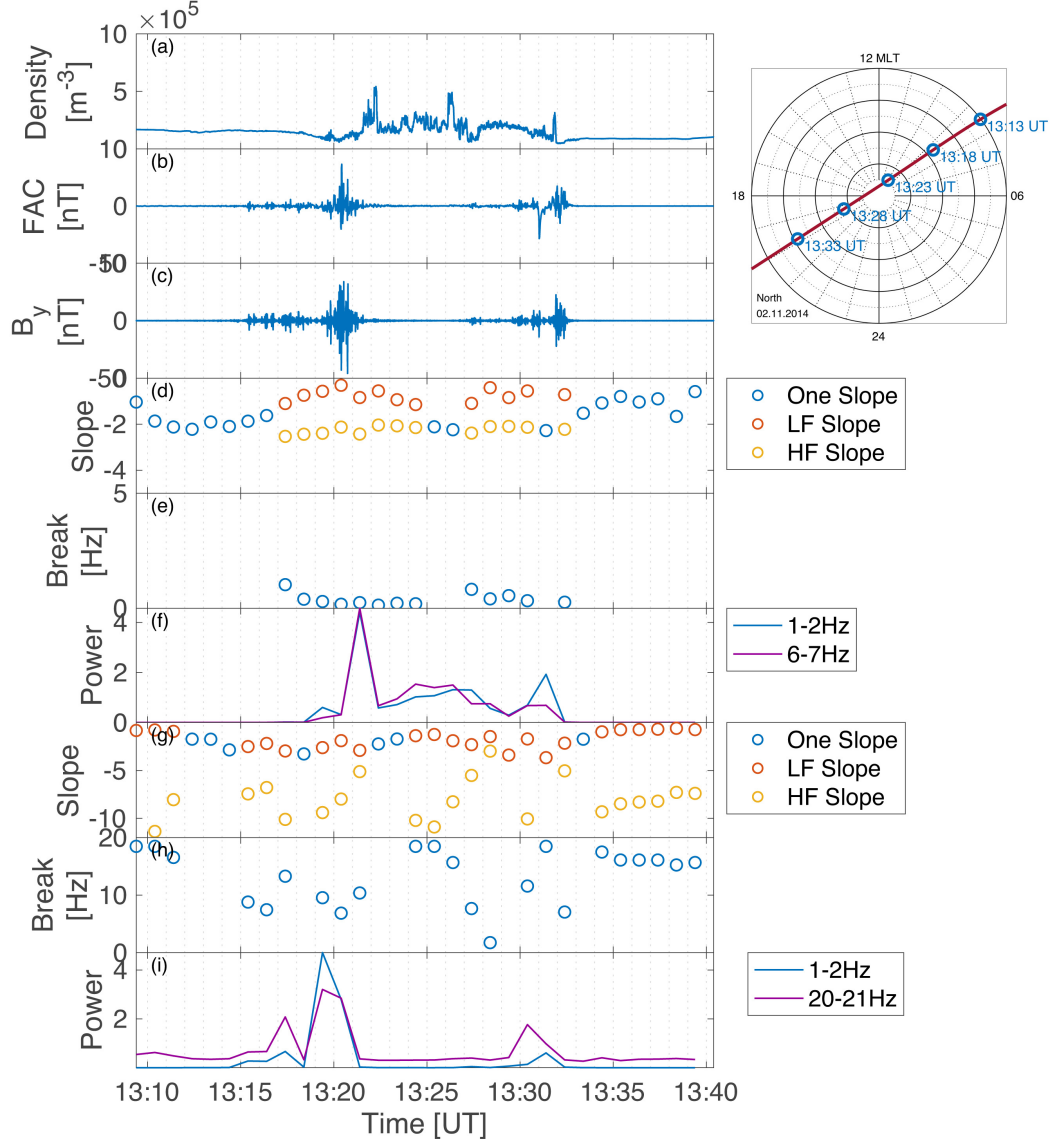
Figure 2. One pass of Swarm A over the polar region in the northern hemisphere on 02.11.2014 between 13:09 UT and 13:41 UT. The panels show the following from top to bottom: The 16 Hz electron density (a), the 1 Hz field-aligned current (b), the 50 Hz y-component of the magnetic field (c), the slopes obtained from the electron density PSD (d) and the corresponding spectral break frequencies (e), the integrated power from the electron density PSD between 1-2 and 6-7 Hz (f), the slopes obtained from the B_y PSD (g) and the corresponding spectral break frequencies (h), the integrated power from the B_y PSD between 4-5 and 20-21 Hz (i).

ble and the integrated power between 1-2 Hz and 6-7 Hz for 1-minute intervals, respectively.

The satellite encounters very little density fluctuations in both midlatitude (ML) regions. This is linked with a single slope and little integrated power in the corresponding power spectra. One way to distinguish the AO from the PC and ML regions is by looking at the FAC graph (panel b) and the magnetic field graph (panel c). When the satellite passes the AO, north of 67° MLAT, the power spectra of the plasma density (panels d and e) start being best described by a double slope instead of a single slope and the integrated power (panel f) rises. Within the PC, recognizable by the region in between the strong fluctuations in the FAC and B_y, the density shows several increases, for example at 13:26 UT, which can be associated with polar cap patches. The strongest density fluctuations occur between 13:21 UT and 13:28 UT. After that, the density fluctuations diminish slightly. While the integrated power from the density PSD (panel f) clearly exhibits peaks within the auroral oval (AO) during strong FAC fluctuations, a third peak can be seen within the PC. While this third peak around 13:26-13:27 UT occurs simultaneously and could thus be linked to the polar cap patch at 13:27 UT, it is notable to mention the two PSD which are described by a single slope rather than a double slope. The slopes from the B_y PSD (panel g) are best described by a double slope throughout the majority of the passing, while the integrated power from the same PSD (panel i) is enhanced within the AO.

For the duration of the time interval chosen to analyze we analyzed 12490 passes over the poles, roughly equally distributed over both hemispheres. This corresponds to about 400.000 power spectra for the density and about the same amount for the magnetic field data.

In order to do a statistical approach, we binned the data into several regions between 50 and 90° MLat in 2° steps and between 0 and 24 hours MLT in 1 hour steps. If the satellites had several passes within a given region, leading to more than one data point within the bin, the mean of all data points within the bin was calculated for the graphs depicting the integrated power of the electron density and B_y, as well as the ROTI data. For the slope probability plots we calculated the chance for a single slope by dividing the number of single slopes by the total number of passes within a bin. The double slope probability was calculated in a similar way. These two quantities were merged into a probability scale ranging from 100 % single slope probability (SS probability) to 100 % double slope probability (DS probability).

3 Results

We used all passes Swarm A and C made between October 2014 and December 2016 where the electron density, magnetic field data and FAC were available. Additionally, we used all passes between January 2020 and December 2022 with the same requirements, as well. The data with low activity did not vary greatly from the high activity data. Additionally, the passes between 2020 and 2022 were limited by the 16 Hz density data which was only collected for short intervals within the given timeframe. Thus, this data can be found in Appendix A for comparison. Figure 3 shows slope probability and integrated power for high solar activity (2014 to 2016) obtained from the electron density PSD. The plot is divided into four seasons from spring to winter in column 1-4, respectively. The first two rows, rows A and B, show the slope probability and integrated power of the northern hemisphere (NH), respectively, while the two bottom rows, rows C and D, show the same quantities for the southern hemisphere (SH). The slope probability ranges from 100 % DS probability (dark red) to 100 % SS probability (dark blue). If it is equally likely to obtain a single or double slope in the corresponding bin, the bin is yellow.

Both the northern and southern hemisphere slope probability (rows A and C) show a seasonal dependency. In local summer the slope probability for a DS throughout the
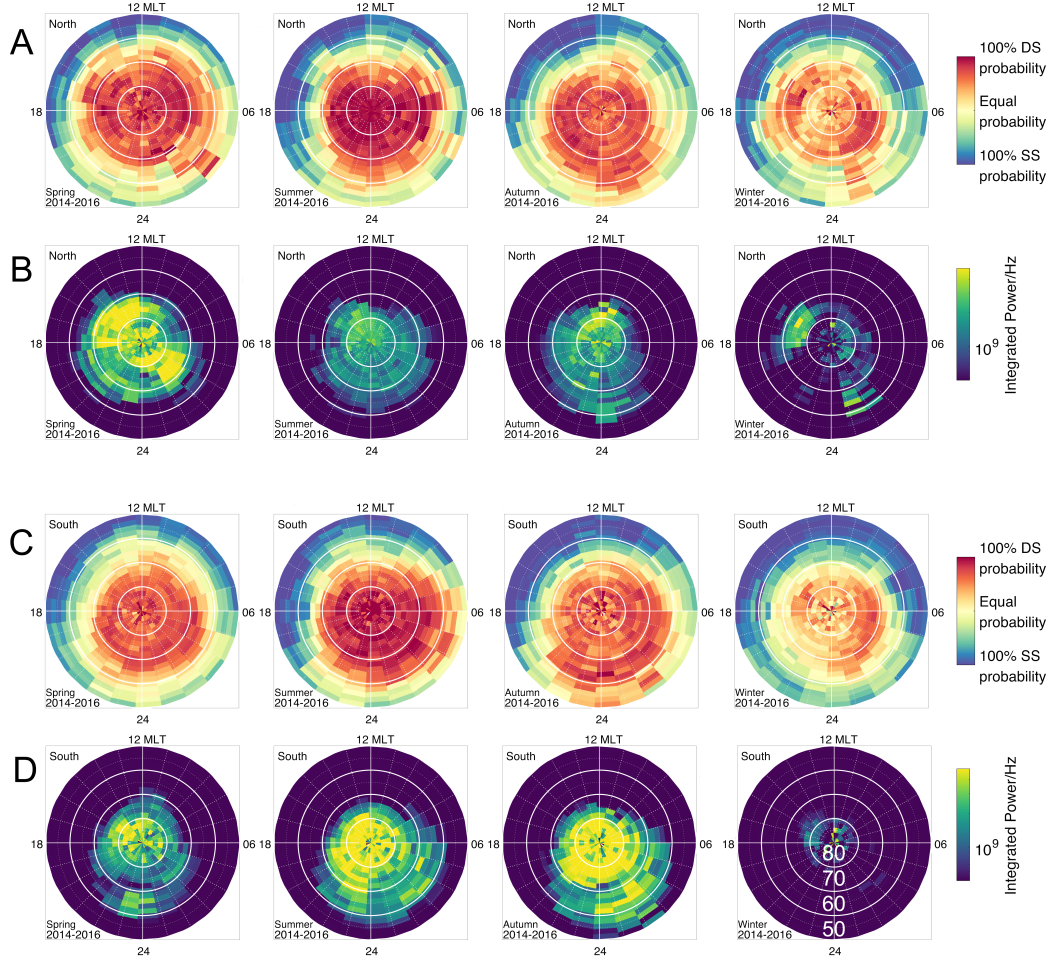
Figure 3. Slope probability and integrated power for the interval between 1-2 Hz obtained from the PSD of the electron density. The four columns contain the four seasons from spring to winter, while the four rows, rows A-D, show the slope probability and integrated power for the northern hemisphere (rows A and B) and for the southern hemisphere (C and D) for high solar activity (years 2014-2016). All seasons are local seasons. The magnetic latitude is indicated on the bottom right plot.

AO, which is typically found in around 70° MLAT, and PC is close to one, especially in the PC. For both spring and autumn, the probability for a double slope is still very close to 1, however, compared to the summer, the probability in the AO becomes higher than in the PC. This ratio grows further during winter time, where it is mostly equally likely in the PC for a spectrum to exhibit a double slope as it is for a single slope, while the probability for a double slope stays high in the AO for all seasons. While a higher DS probability is found mostly throughout the AO and PC regions, the dayside ML below approximately 60° MLAT shows a very high SS probability, which is also the only region where we consistently find a higher probability for a SS than a DS. In the night time below 60° MLAT we rather encounter an equal slope probability. These findings hold true for both northern and southern hemisphere, though the contrast between summer and the other seasons seems to be more pronounced in the SH. Additionally, we find similar results for low solar activity (2020-2022), which can be seen in Appendix A, see figure A1. Furthermore, the autumn season shows a higher double slope probability at lower latitudes for the midnight sector in comparison to the other seasons. Note that all seasons are local seasons, which means that the autumn data from the northern hemisphere corresponds to the same time frame as the spring data of the southern hemisphere. As both hemispheres show a higher double slope probability around midnight for lower latitudes in the autumn, this is not related to a small number of events leading to higher probabilities, but rather is to be related to the season itself.

Row B and D show the integrated power between 1-2 Hz. Again, we find a seasonal dependency, though this time we find differences in the northern and southern hemisphere. In the NH the integrated power is more pronounced around the spring and autumn equinoxes than the summer, with little integrated power throughout the winter. However, the SH has a higher integrated power in summer than spring, though autumn still exhibits the highest power. In both cases, the integrated power in local winter is significantly lower when compared to other seasons. This also holds true for low solar activity in figure A1 B and D. For the slope probability we obtained a lower probability for a double slope in the PC during autumn, spring and winter compared to summer, though the probability in the AO stays high. The integrated power, however, stays elevated in the PC compared to the AO, even if the overall power diminishes. Notable is also the high integrated power northward of 60° MLAT around midnight during spring in the southern hemisphere (bottom left panel), which does not correspond with a higher probability for either a single or double slope. Generally, while both the double slope probability and integrated power are more pronounced throughout the AO and PC, a high integrated power is not necessarily followed by a higher double slope probability.

Another important aspect is the asymmetry between the hemispheres. The slope probability shows a high similarity for all seasons with high probabilities in the summer and diminishing probabilities for the equinoxes and winter for both high and low solar activity. However, the integrated power shows no such resemblances. Generally, the SH summer integrated power is enhanced in comparison to the other seasons, while in the northern hemisphere the integrated power around the equinoxes is more pronounced.

Figure 4 shows the rate of change of TEC index (ROTI) obtained from the IPIR dataset, for the northern and southern hemispheres (row A and B, respectively). The four columns show the four seasons from spring to winter going from left to right. The northern hemisphere shows an elevated ROTI in the spring and autumn mainly in the night side auroral oval and between 70 and 80° MLAT around noon. While the same areas are also enhanced during summer, the overall index is lower than around the equinoxes. Note, that the index in the NH polar cap is generally more enhanced than the index in the ML, though the largest enhancements are found within the AO. The southern hemisphere is generally more enhanced than the NH, though, similar to the electron density results, a difference during seasons can be observed. The local summer and autumn seasons are overall more enhanced than the other seasons, especially within the polar cap. During local spring, ROTI is mainly enhanced within the nightside auroral oval around
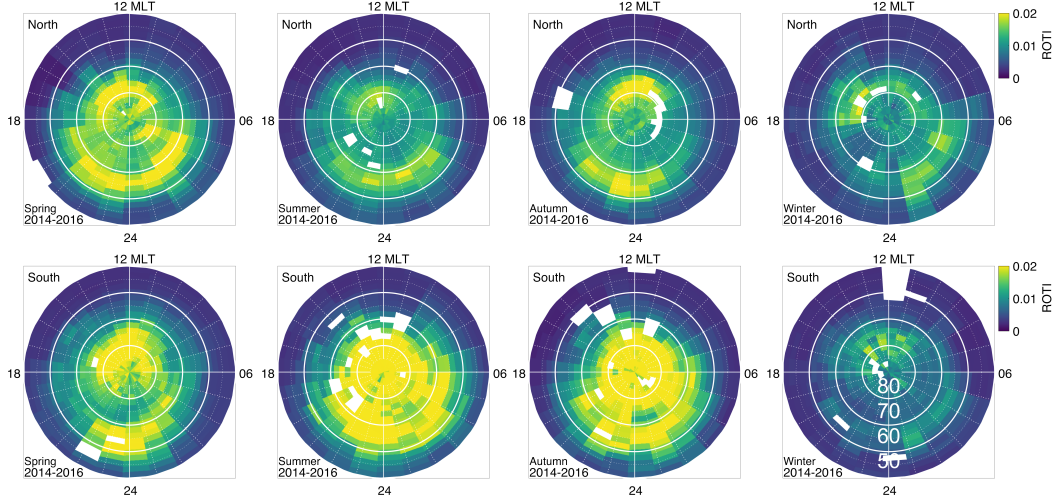
Figure 4. Rate of change of TEC Index (ROTI). The four columns contain the four seasons from spring to winter, while the two rows, rows A-B, show the ROTI for the northern hemisphere and southern hemisphere (rows A and B, respectively) for high solar activity (years 2014-2016). All seasons are local seasons. The magnetic latitude is indicated on the bottom right plot.

midnight and northward of 70° MLAT around noon. For both hemispheres local winter shows comparably low enhancement within all regions.

Figure 5 is similar to figure 3 and shows the slope probability and integrated power obtained from the PSD of the B_y component. The plot is divided into four seasons from spring to winter in column 1-4, respectively. The first two rows, rows A and B, show the slope probability and integrated power of the NH, respectively, while the two bottom rows, rows C and D, show the same quantities for the SH.

In both the northern and southern hemisphere the double slope probability (row A and C) is high in the AO and cusp region, typically found around noon and 75° MLAT. Additionally, we find a higher double slope probability southward of 60° MLAT on the nightside, while the dayside shows an equal probability for single and double slopes southward of 70° MLAT for nearly all plots. Generally, it is either likely that we can find an equal probability or a higher probability for double slopes throughout all plots, only very little bins show a higher probability for a single slope, and if so, the bins are either located on the dayside, in the PC or directly southward of the PC around midnight. This holds true, again, for the slope probabilities during low activity, see figure A2 in Appendix A, though more bins exhibit a single slope probability, however, the single slope probability is still dominant in few bins. Moreover, both autumn graphs (A and C, third plot) show a stronger double slope probability between 60° MLAT and 70° MLAT during midnight.

The integrated power between 1 and 2 Hz (row B and D) is also most elevated in the AO throughout all plots both for high and low activity. While most of the auroral oval exhibits a more or less uniform elevated integrated power, there is higher powers found around 75° MLAT around magnetic noon, thus in the cusp, for several of the plots. While the slope probability shows a strong double slope probability within the midnight section below 60° MLAT, this is not the case for the integrated power.
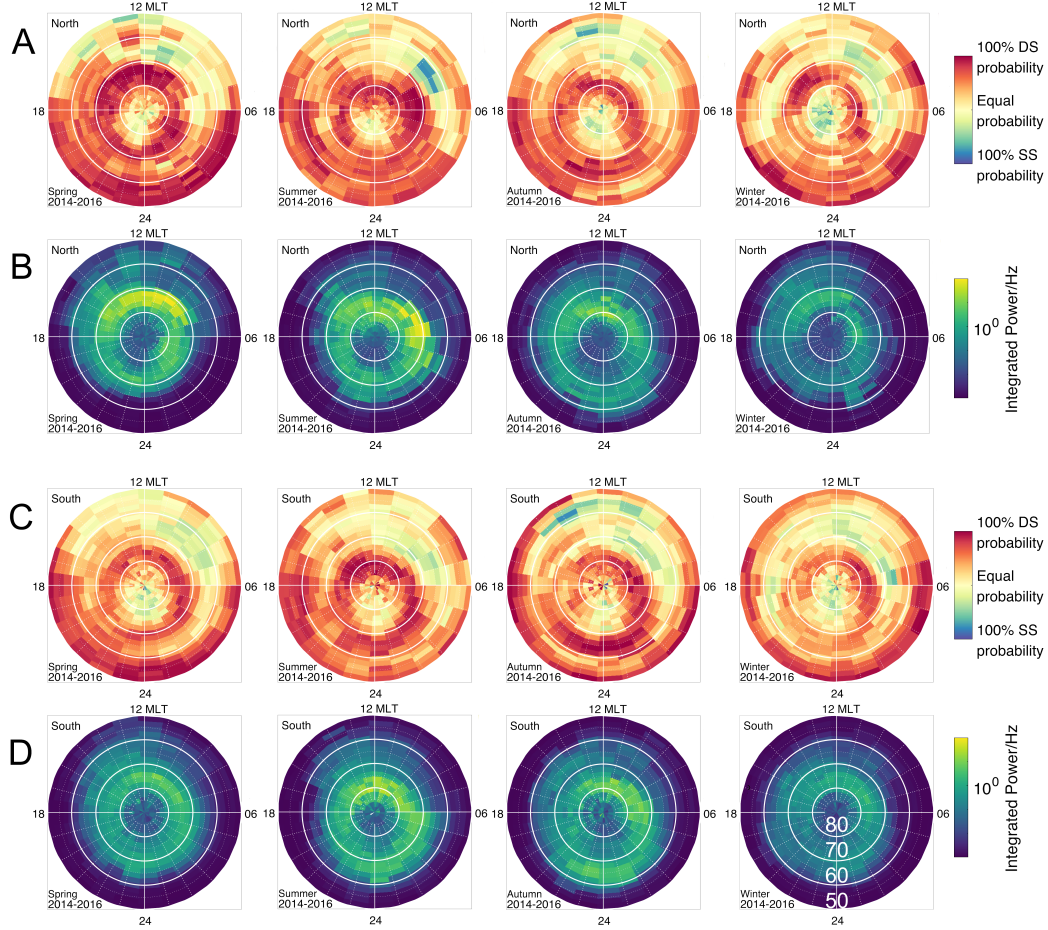
–10–

Figure 5. Slope probability and integrated power for the interval between 1-2 Hz obtained from the PSD of the B_y component. The four columns contain the four seasons from spring to winter, while the four rows, rows A-D, show the slope probability and integrated power for the northern hemisphere (rows A and B) and for the southern hemisphere (C and D) for high solar activity (years 2014-2016). All seasons are local seasons. The magnetic latitude is indicated on the bottom right plot.

4 Discussion

In this study we utilize several years of in-situ measurements from Swarm A and C data in order to investigate a connection between irregularities in the B_y component and strong electron density fluctuations in the polar ionosphere. Additionally, we use ROTI data from the IPIR dataset. We compared the slope probability and integrated power between 1-2 Hz of the electron density PSD in the NH and SH for solar maximum. Both quantities show a seasonal dependency, though not for the same seasons. The slope probability varies with solar EUV radiation, meaning that we find the highest probability for a double slope to describe a power spectrum in local summer months. Close to the equinoxes the probability for a DS becomes less, especially in the polar cap. This tendency becomes even stronger during winter months, where the DS probability is roughly equal to a SS probability for most parts within the PC. These results are consistent with Ivarsen et al. (2021). They have linked the existence of DS to the influence of the SZA, showing a higher DS probability with lower SZA, presenting evidence for a dependency of plasma density irregularities in the polar cap on solar EUV. A higher solar EUV leads to an increase of conductivity in the E-region, which consequently leads to a faster decay of plasma structures in the F-region due to the coupling between both regions (Kelley et al., 1982; Ivarsen et al., 2019; Buschmann et al., 2023; Ivarsen et al., 2023). At this point it is worth mentioning that a quantity of PSD equator-ward of the AO are shallowing out, meaning the second, high-frequency slope is very flat compared to the first slope. This mainly happens in regions where the density is smooth and unstructured. When looking at the slopes of the PSD in a turbulence context, a shallow slope is associated with an energy input in these frequencies. The algorithm that is used for slope detection, however, labels these spectra as single slopes, as the condition $p_2 - p_1 \geq 0.8$ is not met.

The integrated power for the electron density PSD show seasonal dependencies for the NH and SH. The northern hemisphere generally shows a higher power around the equinoxes, while the southern hemisphere additionally exhibits elevated power in local summer. Generally, while the slope probability in the NH and SH are very similar, the integrated power shows no such similarity between the hemispheres and seasons. This suggests a disconnect between the slope probability and the energy deposited in kilometer-scale structures. The higher integrated power around the equinoxes may be explained due to the tilt of the earth's axis and the additionally slanted magnetic field, leading to a better alignment between the earth's magnetic field and that of the solar wind. Generally, the seasonal variation of geomagnetic storms has been ascribed to both axial and equinoctal phenomena, alongside the Russell-McPherron effect (Russell & McPherron, 1973; Cortie, 1912; Gonzalez et al., 1994; Echer et al., 2011). The elevated occurrence of geomagnetic storms and the accompanying precipitating particles can then lead to a higher deposition of energy into lower frequencies, as analyzed here, around the equinoxes. An increased deposition of energy into low frequencies during particle precipitation has as well been described in Buschmann et al. (2023). The enhanced power in the southern hemisphere within the summer months could be caused by the additional offset of the Earth's magnetic field in the SH. The magnetic pole in the SH is more than $8.5°$ farther from the geographic pole in the SH when compared to the NH. This results in higher illumination in the southern polar region. Convection can then lead to a higher structuring within the summer month in the SH (Coley & Heelis, 1998; Noja et al., 2013; Laundal et al., 2017). In local winter, both the NH and SH integrated power show the lowest values throughout the seasons. In addition to the 1-2 Hz interval we have analyzed data in between 0.1-0.6 Hz and 6-7 Hz, corresponding to scale sizes between about 10-80 km and of about 1 km, respectively. Both datasets show similar trends to the analysis of the 1-2 Hz interval, indicating consistent results throughout the scale sizes.

In order to get a better picture of the density structuring within the polar regions, we also analyzed the ROTI data within the same time-frame as the PSD analysis. The overall seasonal variation of the ROTI data aligns with the seasonal variation that we found within the integrated power of the electron density PSD. Additionally, the inter-hemispheric variation that we saw within the integrated power from the density PSD can

348 also be seen within this dataset and is consistent with Jin and Xiong (2020). Generally,
349 the majority of the enhanced ROTI locations also match the integrated power. However,
350 ROTI is much more elevated within the cusp region and nightside AO in the northern
351 hemisphere, while the southern hemisphere shows an additional pronunciation from the
352 cusp into the nightside until the central polar cap, with a small region that exhibits a
353 lower ROTI in the nightside PC. Similar to the integrated power, ROTI also shows a clear
354 distinction between the NH and SH. The low ROTI in winter and higher ROTI values
355 around the equinoxes is consistent with results in (Jin et al., 2019). While ROTI is de-
356 scribed as the standard deviation of the rate of TEC, and thus gives an indication about
357 the structuring in the ionosphere, the integrated power gives an additional insight about
358 the amplitude for a certain frequency range. This implies that the ROTI rather gives
359 an overall indicator for structuring, while the integrated power also shows the strength
360 of the irregularities within the structures. In addition to the PSD analysis of the elec-
361 tron density, we also analyzed the slope probability and integrated power between 1-2 Hz
362 of the y-component of the magnetic field. Both the occurrence rate for a double slope
363 and the integrated power show elevated values within the auroral oval and within the
364 cusp. Additionally, it is more likely for a double slope to occur below 60° MLAT, espe-
365 cially during nighttime, however, there is no elevation within the integrated power. As
366 the y-component of the magnetic field in this study is used as a means for the FAC data,
367 the signal within mid-latitudes is usually low, which may lead to a very low signal within
368 the PSD. Furthermore, as seen in figure 2, the breakpoints in the nightside mid-latitude
369 region is very high and close to the Nyquist frequency for the magnetic field PSD. This
370 adds additional uncertainty for these spectra. Thus, the double slope probability in these
371 regions should be assessed with caution and may likely be a result of noise. Generally,
372 the magnetic field shows a integrated power in a circle around the pole, corresponding
373 to the FAC data, see figure A3. In addition, the highest values are found in the morn-
374 ing sector and the cusp for all seasons and both hemispheres. These enhancements within
375 the FAC in the cusp are co-located with the strong ROTI enhancements as seen in fig-
376 ure 4. This agrees with previous results that show how auroral dynamics within the cusp
377 can be related to irregularities causing strong phase scintillations within GNSS signals
378 (Jin et al., 2015, 2017; Clausen et al., 2016). This also agrees with Fæhn Follestad et al.
379 (2020), who showed that filamentary FACs are co-located with severe phase scintillation
380 within the cusp.

5 Conclusion

382 We present several years of data from the 16 Hz plasma density, the 50 Hz magnetic
383 field data and ROTI data from the IPIR dataset from Swarm A and C. We applied spec-
384 tral analysis to the density and B_y data and did an analysis on the integrated power within
385 the resulting PSD in order to attain a measure of the energy deposited within the cor-
386 responding scales. Additionally, we also considered if the corresponding PSD was best
387 described by a single slope (SS) or a double slope (DS). To put the data into better con-
388 text, we made use of the 1 Hz ROTI data from the IPIR dataset. The data covers the
389 time frame between October 2014 and December 2016, though we also considered data
390 from 2020 to 2022, but due to lower coverage these datasets have been mainly discussed
391 as reference and can be found in Appendix A. We present data from all passings from
392 Swarm satellites A and C poleward of 50° MLat. The data has then been divided by hemi-
393 spheres and into four seasons by taking equal time frames around the equinoxes and sol-
394 stices for each season. We have been able to confirm results from several previously pub-
395 lished studies but also give new insights. The probability for a DS within the plasma den-
396 sity PSD follows a seasonal variation that changes with EUV-radiation within the PC.
397 For both hemispheres we observe the highest DS probability in local summer. Both equinoxes
398 show lower probability, while the winter season shows the lowest probability. The DS prob-
399 ability within the AO is constantly high and is thus independent on solar EUV and rather
400 depends on auroral dynamics. The integrated power within the 1-2 Hz frequency inter-

val also shows a seasonal variation, however, the variation does not correlate to solar EUV radiation, but rather has its strongest values around the equinoxes and the lowest values in winter. Additionally, while the DS probability showed little difference between the hemispheres, the integrated power showed much higher variability, especially within local summer months. This is likely attributed to the large offset of the magnetic pole in the southern hemisphere. The ROTI values showed a similar variation as the integrated power obtained from the plasma density. However, while the integrated power, especially in the NH, showed a similar elevation for the AO and PC, the ROTI values show higher elevation within the midnight auroral oval and within the cusp. The overall seasonal variation of ROTI has been seen before, though this study gives a seasonal climatology of the results. While the integrated power generally gives a measure of the strength of fluctuations and structuring, similar to ROTI. However, the results are limited to certain spatial scales. The integrated power within both hemispheres is mainly enhanced within the PC and AO, though varying in strength. Generally, ROTI shows enhancements within the same regions, however, the midnight AO and the cusp show further heightened values, thus indicating higher structuring within these regions. Additionally we found higher values of the integrated power of B_y within the cusp, co-located with the ROTI data. Overall, the main points were chosen as follows

- The probability to obtain a double slope within the plasma density PSD shows a seasonal dependency on the influence of solar-EUV and little variation between the northern and southern hemisphere. The integrated power within the frequency interval of 1-2 Hz from the same PSD shows a seasonal dependency with higher power during the equinoxes and a strong interhemispheric variation. This suggests a disconnection between the two quantities.
- ROTI data shows similar behavior to the integrated power from the density PSD but shows larger enhancements within the cusp and nightside auroral oval, which may indicate different drivers for instabilities within these regions.
- The strongest fluctuations within B_y have been found within the cusp for all seasons and both hemispheres, and are co-located with strong ROTI values.

This study has significance on the accuracy and further development of GNSS systems and positioning. In order to achieve a larger picture of the breaking down of irregularities in the polar ionosphere, it would be beneficial to use data with a higher sampling rate in order to map the energy contained over a large range of scales.

Appendix A   Additional Data

References

AD, R. (1995). Ionospheric electrodynamics using magnetic apex coordinates. *Journal of geomagnetism and geoelectricity*, *47*(2), 191–212.
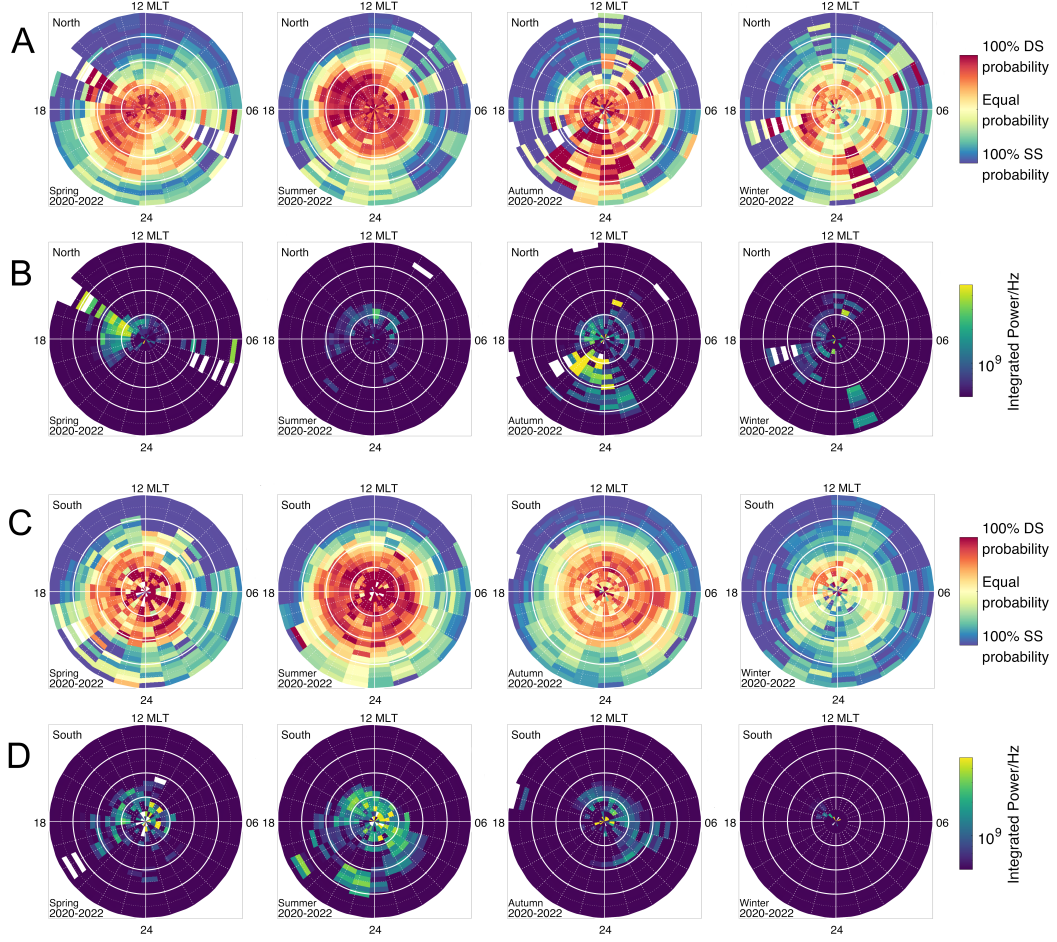
Figure A1. Slope probability and integrated power for the interval between 1-2 Hz obtained from the PSD of the electron density. The four columns contain the four seasons from spring to winter, while the four rows, rows A-D, show the slope probability and integrated power for the northern hemisphere (rows A and B) and for the southern hemisphere (C and D) for low solar activity (years 2020-2022).
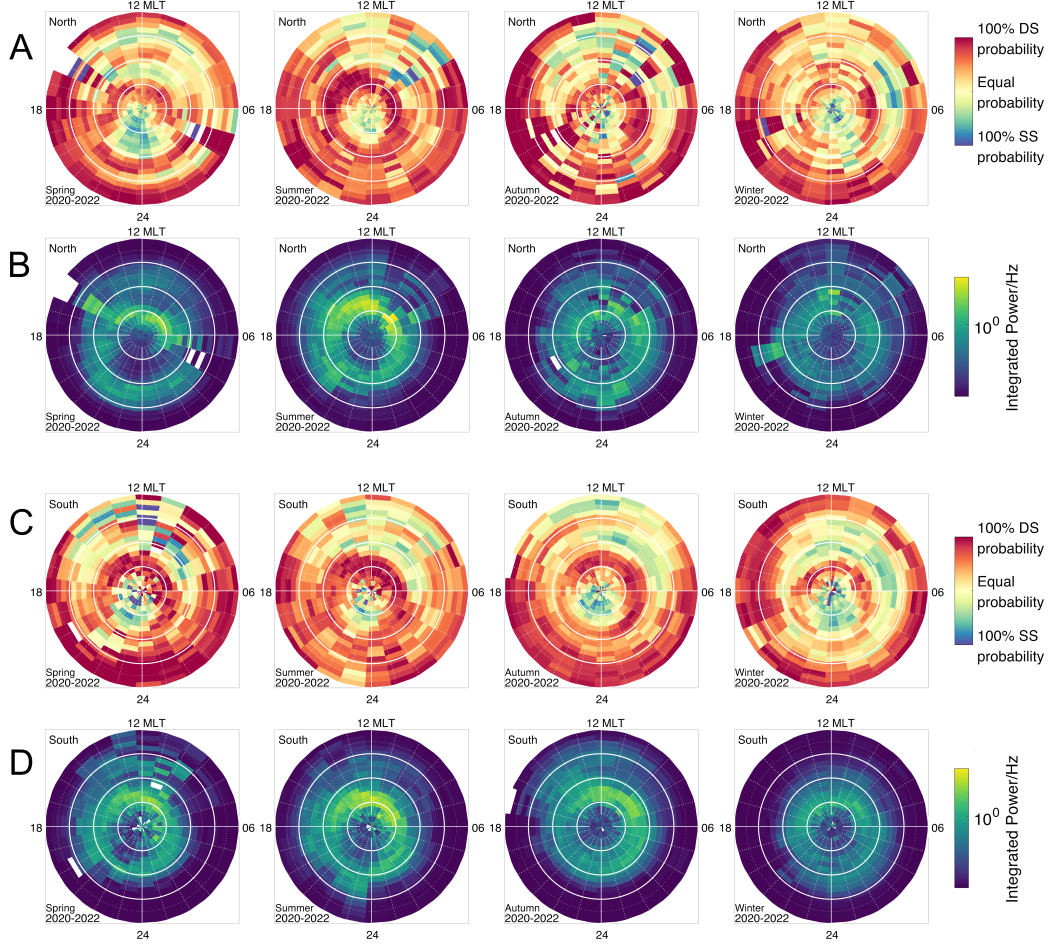
Figure A2. Slope probability and integrated power for the interval between 1-2 Hz obtained from the PSD of the B_y-component. The four columns contain the four seasons from spring to winter, while the four rows, rows A-D, show the slope probability and integrated power for the northern hemisphere (rows A and B) and for the southern hemisphere (C and D) for low solar activity (years 2020-2022).
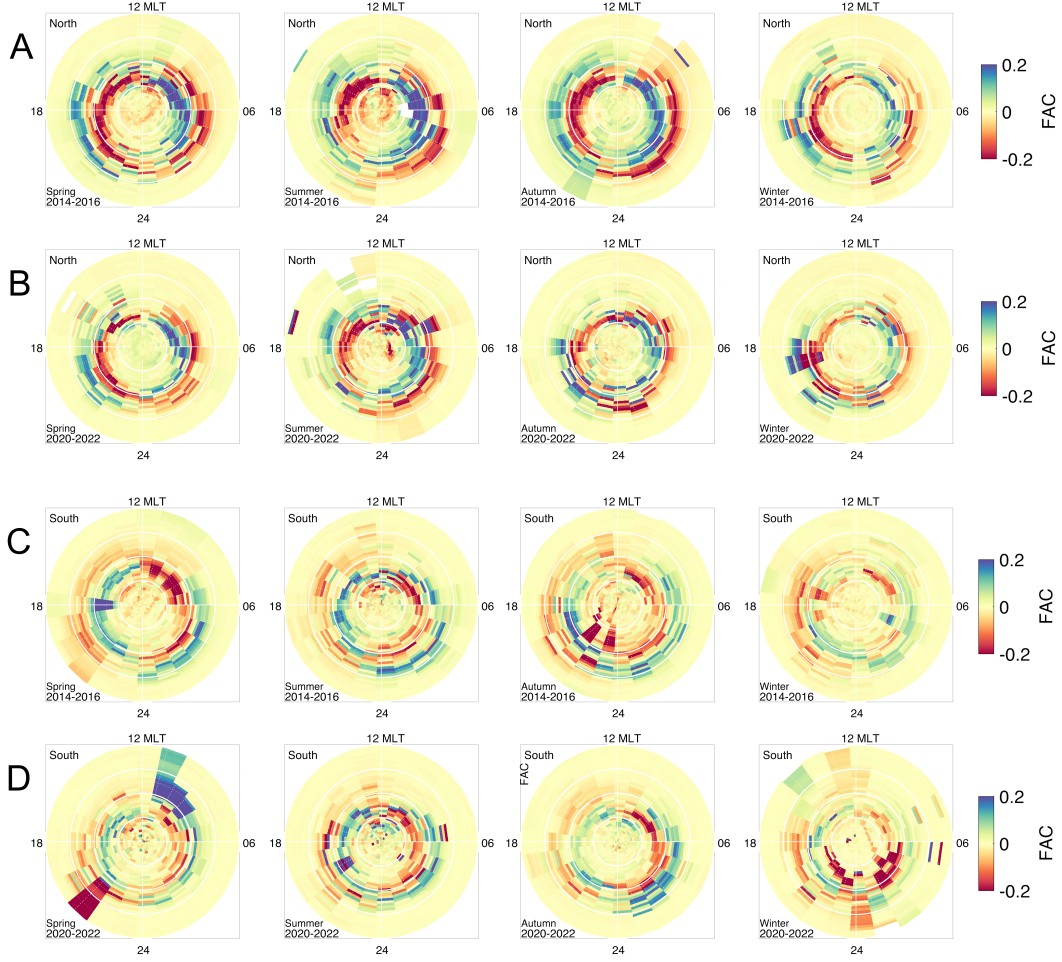
Figure A3. Field aligned current from the 1 Hz Swarm FAC data. The four columns contain the four seasons from spring to winter, while the four rows, rows A-D, show the FAC for the northern hemisphere (rows A and B) for high solar acitvity (row A) and low solar activity (row B), and for the southern hemisphere (C and D) for high solar activity (row C) and low solar activity (row D).

Basu, S., Basu, S., MacKenzie, E., Coley, W., Sharber, J., & Hoegy, W. (1990). Plasma structuring by the gradient drift instability at high latitudes and comparison with velocity shear driven processes. *Journal of Geophysical Research: Space Physics*, *95*(A6), 7799–7818. Retrieved from https://doi.org/10.1029/JA095iA06p07799

Buschmann, L. M., Spicher, A., Clausen, L. B., Marholm, S., & Miloch, W. J. (2023). The role of particle precipitation at different altitudes by in-situ measurements. *Journal of Space Weather and Space Climate*, *13*, 1.

Carlson, H. C. (2012). Sharpening our thinking about polar cap ionospheric patch morphology, research, and mitigation techniques. *Radio Science*, *47*(4). Retrieved from https://doi.org/10.1029/2011RS004946

Carlson, H. C., Pedersen, T., Basu, S., Keskinen, M., & Moen, J. (2007). Case for a new process, not mechanism, for cusp irregularity production. *Journal of Geophysical Research: Space Physics*, *112*(A11). Retrieved from https://doi.org/10.1029/2007JA012384

Chartier, A. T., Huba, J., & Mitchell, C. N. (2019). On the annual asymmetry of high-latitude sporadic f. *Space Weather*, *17*(11), 1618–1626.

Chartier, A. T., Mitchell, C. N., & Miller, E. S. (2018). Annual occurrence rates of ionospheric polar cap patches observed using swarm. *Journal of Geophysical Research: Space Physics*, *123*(3), 2327–2335.

Clausen, L., Moen, J., Hosokawa, K., & Holmes, J. (2016). Gps scintillations in the high latitudes during periods of dayside and nightside reconnection. *Journal of Geophysical Research: Space Physics*, *121*(4), 3293–3309.

Coley, W., & Heelis, R. (1998). Seasonal and universal time distribution of patches in the northern and southern polar caps. *Journal of Geophysical Research: Space Physics*, *103*(A12), 29229–29237.

Cortie, A. (1912). Sun-spots and terrestrial magnetic phenomena, 1898-1911. *Monthly Notices of the Royal Astronomical Society, Vol. 73, p. 52*, *73*, 52.

Crowley, G., Schoendorf, J., Roble, R. G., & Marcos, F. A. (1996). Cellular structures in the high-latitude thermosphere. *Journal of Geophysical Research: Space Physics*, *101*(A1), 211–223. Retrieved from https://doi.org/10.1029/95JA02584

David, M., Sojka, J. J., Schunk, R. W., & Coster, A. J. (2019). Hemispherical shifted symmetry in polar cap patch occurrence: A survey of gps tec maps from 2015–2018. *Geophysical Research Letters*, *46*(19), 10726–10734.

Di Mare, F., Spicher, A., Clausen, L. B. N., Miloch, W. J., & Moen, J. I. (2021). Turbulence and intermittency in the winter cusp ionosphere studied with the ici sounding rockets. *Journal of Geophysical Research: Space Physics*, *126*(8), e2021JA029150. Retrieved from https://doi.org/10.1029/2021JA029150

Echer, E., Gonzalez, W., & Tsurutani, B. (2011). Statistical studies of geomagnetic storms with peak dst- 50 nt from 1957 to 2008. *Journal of Atmospheric and Solar-Terrestrial Physics*, *73*(11-12), 1454–1459.

Emmert, J., Richmond, A., & Drob, D. (2010). A computationally compact representation of magnetic-apex and quasi-dipole coordinates with smooth base vectors. *Journal of Geophysical Research: Space Physics*, *115*(A8).

Fæhn Follestad, A., Herlingshaw, K., Ghadjari, H., Knudsen, D. J., McWilliams, K. A., Moen, J. I., ... Oksavik, K. (2020). Dayside field-aligned current impacts on ionospheric irregularities. *Geophysical Research Letters*, *47*(11), e2019GL086722.

Friis-Christensen, E., Lühr, H., & Hulot, G. (2006). Swarm: A constellation to study the earth's magnetic field. *Earth, planets and space*, *58*, 351–358.

Friis-Christensen, E., Lühr, H., Knudsen, D., & Haagmans, R. (2008). Swarm–an earth observation mission investigating geospace. *Advances in Space Research*, *41*(1), 210–216.

Frisch, U., & Kolmogorov, A. N. (1995). *Turbulence: the legacy of an kolmogorov.*

Cambridge university press.

Gonzalez, W., Joselyn, J.-A., Kamide, Y., Kroehl, H. W., Rostoker, G., Tsurutani, B. T., & Vasyliunas, V. (1994). What is a geomagnetic storm? *Journal of Geophysical Research: Space Physics*, *99*(A4), 5771–5792.

Hosokawa, K., Taguchi, S., Ogawa, Y., & Sakai, J. (2013). Two-dimensional direct imaging of structuring of polar cap patches. *Journal of Geophysical Research: Space Physics*, *118*(10), 6536–6543.

Hysell, D., Kelley, M., Swartz, W., Pfaff, R., & Swenson, C. (1994). Steepened structures in equatorial spread f: 1. new observations. *Journal of Geophysical Research: Space Physics*, *99*(A5), 8827–8840. Retrieved from https://doi.org/10.1029/93JA02961

Ivarsen, M. F., Jin, Y., Spicher, A., & Clausen, L. B. (2019). Direct evidence for the dissipation of small-scale ionospheric plasma structures by a conductive e region. *Journal of Geophysical Research: Space Physics*, *124*(4), 2935–2942. Retrieved from https://doi.org/10.1029/2019JA026500

Ivarsen, M. F., St-Maurice, J.-P., Hussey, G., Spicher, A., Jin, Y., Lozinsky, A., ... Clausen, L. B. (2023). Measuring small-scale plasma irregularities in the high-latitude e-and f-regions simultaneously. *Scientific Reports*, *13*(1), 11579.

Ivarsen, M. F., St-Maurice, J.-P., Jin, Y., Park, J., Miloch, W., Spicher, A., ... Clausen, L. B. (2021). Steepening plasma density spectra in the ionosphere: The crucial role played by a strong e-region. *Journal of Geophysical Research: Space Physics*, *126*(8), e2021JA029401.

Jahn, J.-M., & LaBelle, J. (1998). Rocket measurements of high-altitude spread f irregularities at the magnetic dip equator. *Journal of Geophysical Research: Space Physics*, *103*(A10), 23427–23441. Retrieved from https://doi.org/10.1029/97JA02636

Jin, Y., Kotova, D., Xiong, C., Brask, S. M., Clausen, L. B., Kervalishvili, G., ... Miloch, W. J. (2022). Ionospheric plasma irregularities-ipir-data product based on data from the swarm satellites. *Journal of Geophysical Research: Space Physics*, *127*(4), e2021JA030183.

Jin, Y., Moen, J. I., & Miloch, W. J. (2014). Gps scintillation effects associated with polar cap patches and substorm auroral activity: Direct comparison. *Journal of Space Weather and Space Climate*, *4*, A23. Retrieved from https://doi.org/10.1051/swsc/2014019

Jin, Y., Moen, J. I., & Miloch, W. J. (2015). On the collocation of the cusp aurora and the gps phase scintillation: A statistical study. *Journal of Geophysical Research: Space Physics*, *120*(10), 9176–9191. Retrieved from https://doi.org/10.1002/2015JA021449

Jin, Y., Moen, J. I., Oksavik, K., Spicher, A., Clausen, L. B., & Miloch, W. J. (2017). Gps scintillations associated with cusp dynamics and polar cap patches. *Journal of Space Weather and Space Climate*, *7*, A23.

Jin, Y., Spicher, A., Xiong, C., Clausen, L. B., Kervalishvili, G., Stolle, C., & Miloch, W. J. (2019). Ionospheric plasma irregularities characterized by the swarm satellites: Statistics at high latitudes. *Journal of Geophysical Research: Space Physics*, *124*(2), 1262–1282.

Jin, Y., & Xiong, C. (2020). Interhemispheric asymmetry of large-scale electron density gradients in the polar cap ionosphere: Ut and seasonal variations. *Journal of Geophysical Research: Space Physics*, *125*(2), e2019JA027601.

Kagawa, A., Hosokawa, K., Ogawa, Y., Ebihara, Y., & Kadokura, A. (2021). Occurrence distribution of polar cap patches: Dependences on ut, season and hemisphere. *Journal of Geophysical Research: Space Physics*, *126*(1), e2020JA028538.

Kelley, M. C., Vickrey, J. F., Carlson, C., & Torbert, R. (1982). On the origin and spatial extent of high-latitude f region irregularities. *Journal of Geophysical Research: Space Physics*, *87*(A6), 4469–4475. Retrieved from

https://doi.org/10.1029/JA087iA06p04469

Keskinen, M. J., & Ossakow, S. (1983). Theories of high-latitude ionospheric irregularities: A review. *Radio science*, *18*(06), 1077–1091. Retrieved from https://doi.org/10.1029/rs018i006p01077

Kintner, P. M., Ledvina, B. M., & De Paula, E. (2007). Gps and ionospheric scintillations. *Space weather*, *5*(9). Retrieved from https://doi.org/10.1029/2006SW000260

Kintner, P. M., & Seyler, C. E. (1985). The status of observations and theory of high latitude ionospheric and magnetospheric plasma turbulence. *Space science reviews*, *41*(1), 91–129. Retrieved from https://doi.org/10.1007/bf00241347

LaBelle, J., Kelley, M., & Seyler, C. (1986). An analysis of the role of drift waves in equatorial spread f. *Journal of Geophysical Research: Space Physics*, *91*(A5), 5513–5525. Retrieved from https://doi.org/10.1029/JA091iA05p05513

Laundal, K. M., Cnossen, I., Milan, S. E., Haaland, S., Coxon, J., Pedatella, N., . . . Reistad, J. P. (2017). North–south asymmetries in earth's magnetic field: Effects on high-latitude geospace. *Space Science Reviews*, *206*, 225–257.

Moen, J., Oksavik, K., Abe, T., Lester, M., Saito, Y., Bekkeng, T., & Jacobsen, K. (2012). First in-situ measurements of hf radar echoing targets. *Geophysical Research Letters*, *39*(7). Retrieved from https://doi.org/10.1029/2012GL051407

Moen, J., Oksavik, K., Alfonsi, L., Daabakk, Y., Romano, V., & Spogli, L. (2013). Space weather challenges of the polar cap ionosphere. *Journal of Space Weather and Space Climate*, *3*, A02. Retrieved from https://doi.org/10.1051/swsc/2013025

Moen, J., Walker, I., Kersley, L., & Milan, S. (2002). On the generation of cusp hf backscatter irregularities. *Journal of Geophysical Research: Space Physics*, *107*(A4), SIA–3. Retrieved from https://doi.org/10.1029/2001JA000111

Noja, M., Stolle, C., Park, J., & Lühr, H. (2013). Long-term analysis of ionospheric polar patches based on champ tec data. *Radio Science*, *48*(3), 289–301.

Oksavik, K., Moen, J., Lester, M., Bekkeng, T. A., & Bekkeng, J. K. (2012, November). In situ measurements of plasma irregularity growth in the cusp ionosphere. *Journal of Geophysical Research: Space Physics*, *117*(A11), n/a–n/a. Retrieved from https://doi.org/10.1029/2012ja017835

Ritter, P., Lühr, H., & Rauberg, J. (2013). Determining field-aligned currents with the swarm constellation mission. *Earth, Planets and Space*, *65*(11), 1285–1294.

Russell, C., & McPherron, R. (1973). Semiannual variation of geomagnetic activity. *Journal of geophysical research*, *78*(1), 92–108.

Spicher, A., Clausen, L. B. N., Miloch, W. J., Lofstad, V., Jin, Y., & Moen, J. I. (2017). Interhemispheric study of polar cap patch occurrence based on swarm in situ data. *Journal of Geophysical Research: Space Physics*, *122*(3), 3837–3851.

Spicher, A., LaBelle, J., Bonnell, J. W., Roglans, R., Moser, C., Fuselier, S. A., . . . others (2022). Interferometric study of ionospheric plasma irregularities in regions of phase scintillations and hf backscatter. *Geophysical Research Letters*, *49*(12), e2021GL097013. Retrieved from https://doi.org/10.1029/2021GL097013

Spicher, A., Miloch, W., & Moen, J. (2014). Direct evidence of double-slope power spectra in the high-latitude ionospheric plasma. *Geophysical Research Letters*, *41*(5), 1406–1412. Retrieved from https://doi.org/10.1002/2014GL059214

Tröbs, M., & Heinzel, G. (2006). Improved spectrum estimation from digitized time series on a logarithmic frequency axis. *Measurement*, *39*(2), 120–129.

Tsunoda, R. T. (1988). High-latitude f region irregularities: A review and synthesis. *Reviews of Geophysics*, *26*(4), 719–760. Retrieved from https://doi.org/

614   `10.1029/RG026i004p00719`

615   van der Meeren, C., Oksavik, K., Lorentzen, D. A., Rietveld, M. T., & Clausen,
616   L. B. (2015). Severe and localized gnss scintillation at the poleward edge of
617   the nightside auroral oval during intense substorm aurora. *Journal of Geophys-*
618   *ical Research: Space Physics*, *120*(12), 10–607.

619   Villain, J., Hanuise, C., & Beghin, C. (1986). Arcad3-safari coordinated study of
620   auroral and polar f-region ionospheric irregularities. In *Annales geophysicae*
621   (Vol. 4, pp. 61–68).

622   Wang, H., Lühr, H., & Ma, S. (2005). Solar zenith angle and merging electric field
623   control of field-aligned currents: A statistical study of the southern hemi-
624   sphere. *Journal of Geophysical Research: Space Physics*, *110*(A3).

625   Welch, P. (1967). The use of fast fourier transform for the estimation of power
626   spectra: a method based on time averaging over short, modified periodograms.
627   *IEEE Transactions on audio and electroacoustics*, *15*(2), 70–73.

628   Yeh, K. C., & Liu, C.-H. (1982). Radio wave scintillations in the ionosphere. *Pro-*
629   *ceedings of the IEEE*, *70*(4), 324–360. Retrieved from `https://doi.org/10`
630   `.1109/PROC.1982.12313`